

Solid-State Microwave Magnetometer with Picotesla-Level Sensitivity

Scott T. Alsid^{1,2}, Jennifer M. Schloss^{1,*}, Matthew H. Steinecker¹, John F. Barry¹, Andrew C. Maccabe¹, Guoqing Wang (王国庆)², Paola Cappellaro^{1,2,3} and Danielle A. Braje¹

¹*Lincoln Laboratory, Massachusetts Institute of Technology, Lexington, Massachusetts 02421, USA*

²*Research Laboratory of Electronics and Department of Nuclear Science and Engineering, Massachusetts Institute of Technology, Cambridge, Massachusetts 02139, USA*

³*Department of Physics, Massachusetts Institute of Technology, Cambridge, Massachusetts 02139, USA*

(Received 15 July 2022; revised 5 March 2023; accepted 14 March 2023; published 31 May 2023)

Quantum sensing of low-frequency magnetic fields using nitrogen-vacancy–(N-V) center ensembles has been demonstrated in multiple experiments with sensitivities as low as approximately $1 \text{ pT}/\sqrt{\text{Hz}}$. To date, however, demonstrations of high-frequency magnetometry in the gigahertz regime with N-V diamond are orders of magnitude less sensitive, above the $\text{nT}/\sqrt{\text{Hz}}$ level. Here, we adapt, for microwave frequencies, techniques that have enabled high-performance low-frequency quantum sensors. Using a custom-grown N-V-enriched diamond combined with a noise-cancellation scheme designed for high-frequency sensing, we demonstrate a Rabi-sequence-based magnetometer able to detect microwave fields near 2.87 GHz with a record sensitivity of $3.4 \text{ pT}/\sqrt{\text{Hz}}$. We demonstrate both amplitude and phase sensing and project tunability over a 300-MHz frequency range. This result increases the viability of N-V ensembles to serve as microwave circuitry imagers and near-field probes of antennas.

DOI: [10.1103/PhysRevApplied.19.054095](https://doi.org/10.1103/PhysRevApplied.19.054095)

I. INTRODUCTION

Solid-state spin systems are increasingly favored for quantum sensing [1]. With resonance shifts tied to physical constants [2], these robust systems can be tailored to applications covering a wide range of physical conditions while offering sensitivity and stability [3]. Nitrogen-vacancy (N-V) centers in diamond [Fig. 1(a)] constitute a particularly promising solid-state platform [4], with spin lifetimes exceeding milliseconds [5], high-spatial-resolution optical readout [6], intrinsic vector-sensing capabilities [7], and compatibility with ambient or extreme temperatures [8] and pressures [9]. These advantages have allowed demonstrations of low- and intermediate-frequency sensing applications such as noninvasive detection of neuron action potentials [10], high-resolution NMR [11], single-protein detection [12], elucidation of condensed-matter phenomena [13], mapping of remnant magnetization in geological samples [14], and magnetic navigation [15,16]. Performance in many of these applications is limited by the magnetic field sensitivity of the device [17]. The reported sensitivities of N-V-diamond magnetometers approach or surpass $1 \text{ pT}/\sqrt{\text{Hz}}$ for near-dc fields up to several kilohertz [18–20], and tens of $\text{pT}/\sqrt{\text{Hz}}$ for ac fields from roughly 100 kHz to a few megahertz [11,21,22].

Although N-V-diamond-magnetometry efforts have traditionally focused on sensing submegahertz fields, operation at microwave (MW) frequencies could expand the application space to include imaging of MW-circuitry components [23], antenna characterization [24], and wireless communications [25,26]. To date, however, demonstrated N-V-diamond-based sensitivities at MW frequencies are orders of magnitude worse than those achieved at low frequency, with reported values in the tens of $\text{nT}/\sqrt{\text{Hz}}$ range or above [27,28]. This poor sensitivity results primarily from the use of small N-V ensembles as well as from low fluorescence collection efficiency, poor noise cancellation, and inhomogeneous MW delivery. Dynamical decoupling techniques designed to improve ac magnetometry sensitivity become constrained by the available MW power, especially for large N-V ensembles, limiting their use for sensing gigahertz fields. Techniques to overcome this power limitation, such as concatenated continuous decoupling [29,30] and continuous or pulsed Mollow absorption [31–33], require multiple highly uniform rf control fields, introducing added complexity and homogeneity requirements that are difficult to achieve over large N-V interrogation volumes.

Here, we demonstrate a high-frequency N-V-diamond magnetometer tuned to detect amplitude modulation of a 2.863-GHz MW field. In contrast to complicated pulse schemes for gigahertz field detection including strong-field dynamical decoupling and pulsed Mollow triplet protocols,

*jennifer.schloss@ll.mit.edu

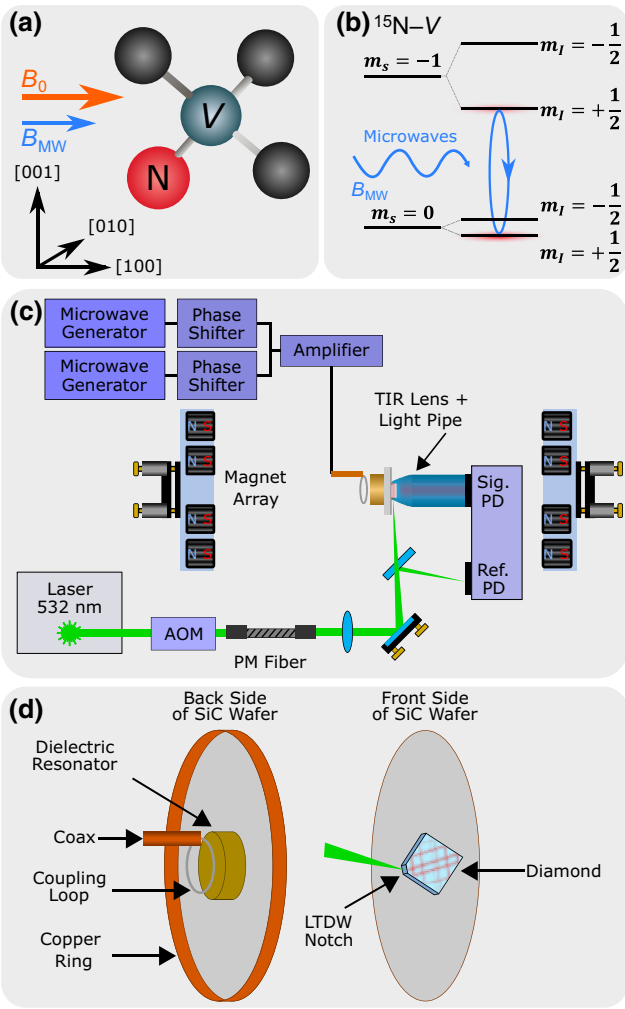


FIG. 1. The experimental setup for Rabi magnetometry using N-V centers in diamond. (a) The N-V center. The static field B_0 and microwave (MW) field B_{MW} are aligned along the $\langle 100 \rangle$ direction of the diamond, projecting equally onto (and transverse to) all four crystallographic axes, resulting in the same resonance frequency and equal MW driving strength for all four N-V orientations. (b) The energy-level diagram for $^{15}\text{N}-V$, showing a resonant MW field driving Rabi oscillations between the $|m_s = 0, m_I = +\frac{1}{2}\rangle$ and $|m_s = -1, m_I = +\frac{1}{2}\rangle$ states. (c) A schematic of the experimental apparatus, including the acousto-optic modulator (AOM), polarization maintaining (PM) fiber, total-internal-reflection (TIR) lens, and signal and reference photodiodes (PDs). (d) A detailed schematic of the silicon carbide (SiC) diamond mount and MW delivery system. The diamond has a small notch cut on the corner to enable a light-trapping diamond-waveguide (LTDW) geometry.

the sensor employs a simple Rabi-magnetometry sequence. Sensitivity to nonmagnetic noise is mitigated by inverting and subtracting the magnetometry signal from consecutive measurements using an additional MW pulse. Combining this scheme with recently demonstrated improvements in optical collection efficiency, laser noise cancellation, and

uniform MW delivery in a low-strain long-dephasing-time diamond [20], the resultant device exhibits a sensitivity of $3.4 \text{ pT}/\sqrt{\text{Hz}}$ for amplitude modulation of a MW carrier over the 100 Hz to 3.3 kHz band.

II. RABI MAGNETOMETRY

When an ideal two-level system is driven by a near-resonant magnetic field [34,35], the population oscillates between the two states $|0\rangle$ and $|1\rangle$ such that the population $P_{|1\rangle}$ is given by the Rabi formula,

$$P_{|1\rangle}(\tau) = \frac{\Omega^2}{\Omega^2 + \delta^2} \sin^2 \left(\frac{\sqrt{\Omega^2 + \delta^2} \tau}{2} \right), \quad (1)$$

where for the frequency ω of the driving field, $\delta = \omega - \omega_0$ is the detuning from the resonance frequency ω_0 and τ is the duration of the driving field. For a coherent MW field B_{MW} , we have the Rabi frequency $\Omega \sim \gamma B_{\text{MW}}$, where γ is the gyromagnetic ratio ($\gamma = 2\pi \times 2.8 \text{ MHz/G}$ for an electron spin).

Rabi magnetometry exploits these population oscillations: small changes in the near-resonant magnetic field amplitude cause the observed oscillation frequency to vary. This variation can be detected by sweeping τ and recording a set of Rabi fringes to determine changes in Ω . Alternatively, τ may be fixed and the signal monitored to detect sufficiently small changes in $P_{|1\rangle}$. While Eq. (1) describes the ideal behavior, Rabi oscillations in a real ensemble decay at a characteristic time scale $T_{2\rho}$ [36], which is the driven-evolution analog of the free-evolution dephasing time T_2^* [37]. The observed value of $T_{2\rho}$ depends on various dephasing mechanisms in the diamond lattice and spatial inhomogeneities in the drive-field intensity [29].

The Rabi-magnetometry scheme employed here consists of a resonant MW field applied to an ensemble of N-V centers in diamond [see Figs. 1(a) and 1(b)] for fixed duration τ , followed by spin-state-dependent optical readout [35]. Monitoring the output signal for each experimental repetition allows amplitude changes in the MW field over time to be measured. The shot-noise-limited MW magnetic field sensitivity η_{shot} of a Rabi magnetometer using an ensemble of N spin defects is given by [38]

$$\eta_{\text{shot}} \approx \frac{\sqrt{2}}{\gamma} \frac{1}{F_\perp} \frac{1}{\sqrt{N n_{\text{avg}}}} \frac{1}{Ce^{-(\tau/T_{2\rho})^p}} \frac{\sqrt{\tau + t_O}}{\tau}. \quad (2)$$

Here, C is the fluorescence contrast between spin states, n_{avg} is the average number of photons collected per N-V per measurement, F_\perp is the projection of the applied MW magnetic field on the plane perpendicular to the N-V axis, and p is a stretched exponential parameter. The overhead time t_O is the duration of any additional steps in the sequence beyond the MW pulse, including optical initialization and readout. Assuming an optimal choice of τ , the

performance of the device depends on the measurement contrast C , the value of $T_{2\rho}$, the number of N-Vs addressed, and the value of n_{avg} [17].

III. EXPERIMENTAL DESIGN

We now highlight experimental design choices to achieve high-performance magnetometry. The experimental setup is shown schematically in Fig. 1(c). This device is modified from the low-frequency magnetometer in Ref. [20] (for additional experimental setup details pertinent to the present demonstration, see the Supplemental Material [38]). The sensor uses a $3 \text{ mm} \times 3 \text{ mm} \times 0.62 \text{ mm}$ single-crystal diamond with $\langle 100 \rangle$ sides and an approximately $70\text{-}\mu\text{m-thick}$ ^{15}N -doped layer, referred to as the N-V layer. The diamond is adhered to a SiC wafer, which acts as a heat sink. Laser light at 532 nm excites N-Vs throughout the N-V layer and the resulting N-V fluorescence is collected by a photodiode [4,39,40]. A 2.23-G bias field splits out the N-V electron spin resonances [41–43], allowing the $|m_s = 0, m_I = +\frac{1}{2}\rangle \leftrightarrow |m_s = \pm 1, m_I = +\frac{1}{2}\rangle$ transitions to be resolved spectroscopically.

The diamond is custom grown and the $70\text{-}\mu\text{m-thick}$ N-V layer exhibits a measured 99.998% ^{12}C purity [44,45]. The diamond is grown using the ^{15}N isotope. The $^{15}\text{N-V}$ centers exhibit only two hyperfine features per spin resonance and a larger splitting compared to the $^{14}\text{N-V}$ center, which has three hyperfine features. A single MW tone can thus drive a larger fraction of the $^{15}\text{N-V}$ population and is less likely to induce off-resonant driving of other hyperfine features. Moreover, the diamond exhibits strain variation of less than $2\pi \times 10 \text{ kHz}$ [46]. This yields a $T_2^* \approx 9 \text{ }\mu\text{s}$ dephasing time [20], which is longer than the typical $T_2^* \lesssim 1 \text{ }\mu\text{s}$ encountered in N-V-ensemble magnetometry [17]. The resulting resonance line width is $\Gamma = 2/T_2^* \approx 2\pi \times 35 \text{ kHz}$. The narrow ensemble line width results in an extended $T_{2\rho}$ by (a) reducing the spread of individual N-V detunings from the MW-drive frequency and (b) enabling the N-V ensemble to be driven effectively at a lower Rabi frequency, reducing the spread of MW field strengths across the ensemble due to any MW inhomogeneity.

Our device employs the light-trapping diamond-waveguide (LTDW) technique [47], which excites N-Vs throughout the $3 \text{ mm} \times 3 \text{ mm} \times 70 \text{ }\mu\text{m}$ N-V-doped volume [Fig. 1(d)]. The fluorescence collection efficiency is increased to approximately 75–95% by surrounding the diamond with a total-internal-reflection lens [20]. In addition, laser light is sampled immediately prior to entering the diamond and is directed to a reference photodiode for common-mode noise cancellation [38].

Both the bias magnetic field B_0 and the MW field B_{MW} are oriented normal to the $\{100\}$ face of the diamond. B_0 projects equally onto all four N-V symmetry axes [see Fig. 1(a)], splitting the $|m_s = 0\rangle \leftrightarrow |m_s = \pm 1\rangle$ transitions

equally. Meanwhile, B_{MW} projects equally onto the planes transverse to the four N-V axes. As a result, all N-V classes may be addressed with a single MW tone at the same Rabi frequency. Because the laser excites N-Vs throughout the N-V layer, it is necessary to minimize static and MW field gradients over the entire N-V-doped volume to avoid degrading $T_{2\rho}$ [48]. The bias-magnet arrangement is designed to minimize static field gradients, while the sensor head incorporates only nonmagnetic materials and limits the use of conductive materials where possible to avoid attenuating high-frequency magnetic fields [49]. Inhomogeneities in B_{MW} are suppressed by coupling MWs from a shorted coaxial cable to a dielectric resonator [50] to achieve a greater than 90% uniformity [51] over the $^{15}\text{N-V}$ layer (see the Supplemental Material [38]).

A single Rabi sequence begins with optical initialization of the N-V ensemble, followed by application of a resonant MW pulse of duration τ and finally optical readout of the N-V state. This process can be repeated while varying τ to observe the Rabi oscillations and decay envelope. In some Rabi-magnetometry implementations [28], each Rabi sequence is followed by a reference sequence with no MWs applied. The signal from the Rabi measurement is then normalized using the signal from the reference sequence, as shown in Fig. 2(a). This “on-off” subtraction protocol suppresses low-frequency noise at the expense of reduced measurement bandwidth and signal [52–54], as half of all measurements produce zero contrast. To improve the signal-to-noise ratio (SNR), we design and implement a subtraction scheme that consists of repeated Rabi sequences performed with and without a π pulse applied before the Rabi drive pulse; the signals from successive sequences are then subtracted to produce the magnetometry signal, as shown in Fig. 2(b). This “ π -pulse” subtraction scheme mitigates the signal reduction while still suppressing low-frequency noise.

The MW field drives a transition to the hyperfine-resolved $|m_s = -1, m_I = +\frac{1}{2}\rangle$ state [55,56] but the near-degeneracy of the $|m_s = 0, m_I = -\frac{1}{2}\rangle$ and $|m_s = 0, m_I = +\frac{1}{2}\rangle$ hyperfine ground states in a small static field [57] complicates the interpretation of the measured Rabi oscillations [58]. The Larmor precession between these near-degenerate states results in a modulation of the overall Rabi-oscillation signal, as seen in Fig. 2(c). The π -pulse subtraction scheme suppresses this hyperfine-mediated modulation arising from the presence of the ^{15}N nucleus in the $^{15}\text{N-V}$ center [59,60], which also allows a more robust determination of $T_{2\rho}$ (see the Supplemental Material [38]).

IV. MAGNETIC FIELD SENSITIVITY

The Rabi frequency that optimizes the sensitivity in Eq. (2) is set by a balance of contrast C and driven coherence time $T_{2\rho}$. Lowering Ω increases $T_{2\rho}$ by reducing the effects of MW field gradients and noise but also degrades the

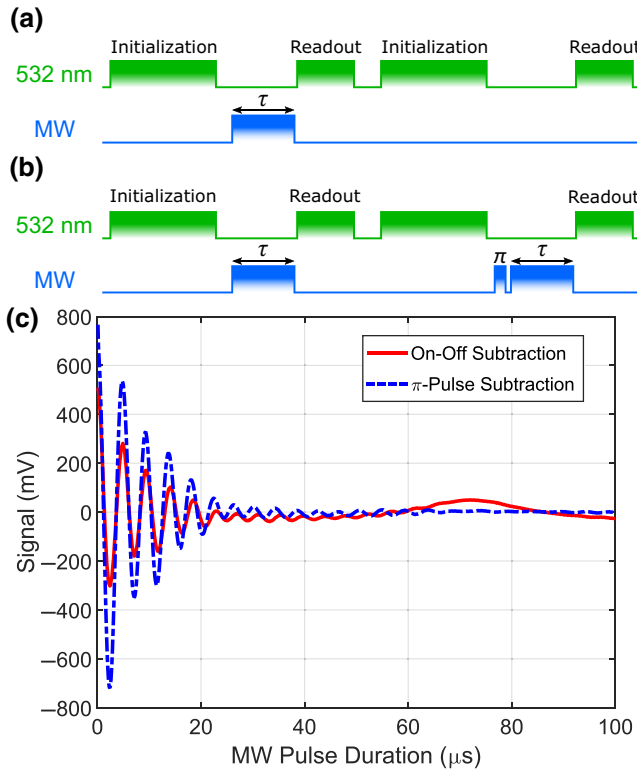


FIG. 2. Noise cancellation. (a) The on-off subtraction protocol consists of two subtracted sequences with a MW drive only in the first sequence. (b) The π -pulse subtraction protocol consists of two subtracted Rabi sequences, where the second sequence contains an additional MW π pulse. While both protocols help eliminate low-frequency noise, the π -pulse protocol maximizes the magnetometry measurement signal-to-noise ratio (SNR) and suppresses the ^{15}N hyperfine modulation observed in the Rabi oscillations. (c) Rabi oscillations at 220 kHz for each subtraction protocol, using a resonant drive field. The π -pulse protocol suppresses the hyperfine-mediated modulation, allowing for a straightforward extraction of $T_{2\rho}$ via a decaying sinusoid fit.

contrast C , as a smaller fraction of the inhomogeneously broadened ensemble is addressed. To quantify this balance, we derive a figure of merit $F(\Omega, \tau)$ from Eq. (2),

$$F(\Omega, \tau) = C(\Omega) e^{-\tau/T_{2\rho}(\Omega)} \frac{\tau}{\sqrt{\tau + t_0}}, \quad (3)$$

where τ is the duration of a MW pulse with intensity Ω ; $t_0 = 44.8 \mu\text{s}$ is the sequence overhead time due to the laser initialization and readout pulses, the π pulse, and electronic dead time; and $C(\Omega)$ and $T_{2\rho}(\Omega)$ are the measured contrast and dephasing time, respectively, as functions of the Rabi frequency. Here, maximizing $F(\Omega, \tau)$ optimizes the sensitivity (minimizes the value of η).

We measure a series of Rabi-oscillation curves, sweeping τ from 0 to 100 μs in a fixed-length Rabi sequence for a range of values of Ω . We fit each curve to extract $T_{2\rho}$ and C (see Fig. S4 of the Supplementary Material [38]); the

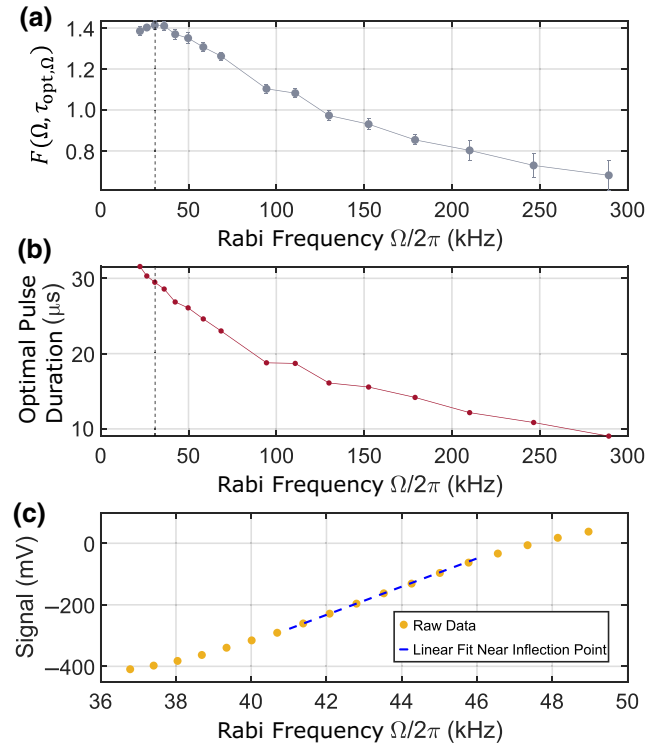


FIG. 3. The Rabi-frequency dependence of the key device parameters. (a) The sensitivity figure of merit $F(\Omega, \tau_{\text{opt},\Omega})$ at different MW field strengths for a 100 μs Rabi-pulse sequence, which produces the initial estimate of the optimal Rabi frequency Ω_{opt} . (b) The optimal MW pulse duration $\tau_{\text{opt},\Omega}$ calculated to maximize the figure of merit $F(\Omega, \tau_{\text{opt},\Omega})$ for a given Rabi frequency Ω . The value corresponding to the maximum value of $F(\Omega, \tau_{\text{opt},\Omega})$ sets the MW pulse length for the magnetometry sequence. (c) Empirical determination of the optimum Rabi frequency for a fixed MW duration, $\tau = 30 \mu\text{s}$. The N-V-ensemble fluorescence signal is most sensitive to changes in the applied MW field at the point of steepest slope, $\Omega_{\text{opt}} = 2\pi \times 42.8 \text{ kHz}$. The peak-to-peak signal in (c) exceeds that of Fig. 2(c) for $\tau = 30 \mu\text{s}$ due to the smaller MW field and increased $T_{2\rho}$, consistent with (b).

long maximum Rabi pulse of 100 μs is to ensure an accurate fit of $T_{2\rho}$ and C . Using these measurements and Eq. (3), we determine the optimal MW pulse duration $\tau_{\text{opt},\Omega}$ that maximizes $F(\Omega, \tau)$ for a given $C(\Omega)$ and $T_{2\rho}(\Omega)$. Plotting the values of $F(\Omega, \tau_{\text{opt},\Omega})$ as a function of Ω , we find that $\Omega = 2\pi \times 31 \text{ kHz}$ maximizes the figure of merit $F(\Omega, \tau_{\text{opt},\Omega})$ with $\tau_{\text{opt},\Omega} = 30 \mu\text{s}$, as shown in Figs. 3(a) and 3(b).

We then generate a new Rabi sequence with the time between the initialization and readout pulses reduced from 100 μs to 30 μs , eliminating unnecessary overhead time. We observe that this change in sequence duration slightly alters the experimental conditions, resulting in a new optimal value of Ω . We perform this final optimization step by

varying Ω for the shorter, $\tau = 30 \mu\text{s}$, sequence to maximize the slope of the fluorescence signal S , $|\partial S/\partial\Omega|$, as shown in Fig. 3(c). This optimal Rabi frequency Ω_{opt} maximizes the response to a given magnetic field; we find that the $\tau = 30 \mu\text{s}$ sequence exhibits an optimal Rabi frequency of $\Omega_{\text{opt}} = 2\pi \times 42.8 \text{ kHz}$. The linear regime as indicated in Fig. 3(c) is about $2\pi \times 4 \text{ kHz}$, which corresponds to about 250 nT (for a detailed description of the operating regimes of the sensor, see Section S5.D of the Supplemental Material [38]).

The $\tau = 30 \mu\text{s}$ Rabi sequence is performed at a 13.23-kHz rate. With the π -pulse subtraction protocol, magnetometry data are collected at a 6.615-kHz rate. The measurement is run continuously to yield a 1-s-length fluorescence time series. Each time series is Fourier transformed with rectangular windowing to produce a single-sided amplitude spectral density (ASD) with 1-Hz-wide frequency bins up to 3.3075 kHz.

We next determine the sensitivity η for a modulation frequency band of interest. Assuming white Gaussian noise in this band, the sensitivity can be expressed as

$$\eta = \frac{\sigma_B}{\sqrt{2f_{\text{ENBW}}}}, \quad (4)$$

where σ_B is the standard deviation of the zero-signal magnetic field time trace over the equivalent noise bandwidth f_{ENBW} [7]. We first calculate the standard deviation σ_S of a time series of fluorescence measurements by applying a 100-Hz brick-wall high-pass filter (such that $f_{\text{ENBW}} = 3207 \text{ Hz}$) on the amplitude spectral density and then finding the root-mean-square average. The standard deviation σ_S is then divided by the slope $|\partial S/\partial\Omega|$ and γ to express the standard deviation in magnetic field units, σ_B . Taking into account the projection of the $\langle 100 \rangle$ -directed MW field onto the plane perpendicular to each $\langle 111 \rangle$ N-V axis, the sensitivity is

$$\eta = \frac{\sqrt{3}}{\gamma |\partial S/\partial\Omega|} \frac{\sigma_S}{\sqrt{2f_{\text{ENBW}}}}. \quad (5)$$

Figure 4(a) shows a calibrated amplitude spectral density for a Rabi-magnetometry measurement with $\Omega = 2\pi \times 42.8 \text{ kHz}$ and $\omega = 2\pi \times 2.863 \text{ GHz}$. The rms average sensitivity in the 100–3307 Hz band is $3.4 \text{ pT}/\sqrt{\text{Hz}}$, indicating that this magnetometer operates close to the shot-noise limit of $1.34 \text{ pT}/\sqrt{\text{Hz}}$ (as calculated in the Supplemental Material [38]).

As a demonstration of our N-V-ensemble Rabi magnetometer, we apply and detect amplitude- and phase-modulated test signals, as commonly used in a number of near- and far-field communications protocols [26,61]. The application of a small resonant MW field δB_{MW} in addition to the MW driving field B_{MW} modifies the Rabi frequency, which causes a fluorescence change as illustrated in Fig. 3(c). Assuming that B_{MW} and δB_{MW} lie along

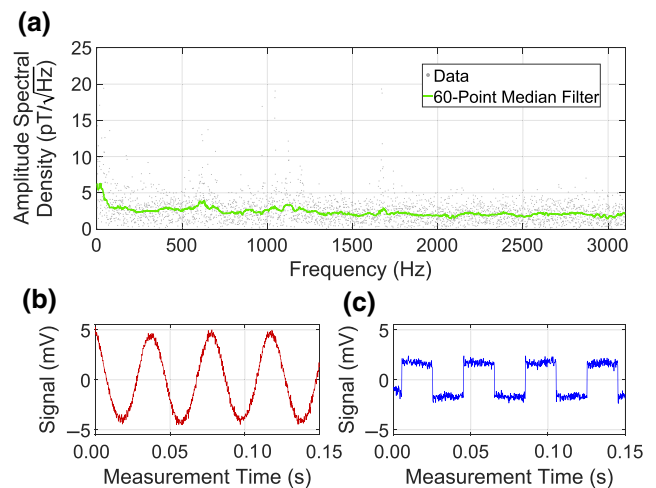


FIG. 4. Rabi magnetometry. (a) The amplitude spectral density of a 1-s measurement with no signal field applied. The units are calibrated by the slope and the N-V gyromagnetic ratio as discussed in the text. (b) Magnetometry signal from a separate $\delta B_{\text{MW}} = 4.4 \text{ nT}$ 25-Hz amplitude-modulated magnetic field with 100% modulation depth. (c) Magnetometry signal from a separate $\delta B_{\text{MW}} = 2.2 \text{ nT}$ 25-Hz phase-modulated magnetic field with a $\pi/4$ phase deviation.

the same axis, the resulting Rabi frequency will fall in the range $\gamma(B_{\text{MW}} \pm \delta B_{\text{MW}})/\sqrt{3}$ [38]. Any amplitude or phase modulation present on δB_{MW} will likewise modulate the resulting N-V fluorescence. Figures 4(b) and 4(c) show an example of a sine-wave amplitude modulation and square-wave phase modulation. For digital modulation in particular, if fluorescence thresholds are associated with a logical 0 and 1, then basic communication protocols, such as binary-phase shift keying, can easily be implemented [26].

V. DISCUSSION AND OUTLOOK

In conclusion, we demonstrate a N-V-diamond MW magnetometer achieving $3.4 \text{ pT}/\sqrt{\text{Hz}}$ sensitivity, near the shot-noise limit of the device. Additional optimization is expected to yield further performance improvements. For example, longer driven coherence times $T_{2\rho}$ can be achieved by increasing the MW homogeneity over the sensor volume through better matching of the dielectric resonator and diamond-sample geometries. Furthermore, the application of additional control fields can suppress noise in the Rabi drive field [30,32,62]. Finally, irradiation and annealing of the diamond can increase the number of N-V centers interrogated while minimally affecting the decoherence time [63].

This technique can be adapted to different high-frequency regimes. A stronger applied static field B_0 can allow extension of this sensing technique to both higher and lower frequencies [64]; an approximately 50-G

increase in B_0 is expected to shift the resonance frequency by ± 150 MHz and allow magnetometry without substantial loss of sensitivity. Further increases in B_0 are expected to degrade performance, e.g., due to bias-field gradients, precluding high-sensitivity Rabi magnetometry down to the megahertz regime. However, the spin-locking protocol [65], where the MW-drive Rabi frequency is matched to the frequency of the target field, can allow detection of fields with frequencies in the hundreds of kilohertz to few megahertz with a modest bias field. Sensing arbitrary frequencies, e.g., in the hundreds of megahertz, can be accomplished using a technique called quantum frequency mixing [66]. This protocol mixes an ac bias field with the desired signal field such that the frequency sum or difference matches the N-V energy-level splitting, also without requiring large bias fields.

The demonstrated pT/ $\sqrt{\text{Hz}}$ sensitivity shows that, with adequate engineering and optimization, sensors based on N-V ensembles are capable of sensing MW magnetic fields with comparable performance to that demonstrated for static and low-frequency fields. The reported sensitivity is orders of magnitude better than previous diamond-based sensors operating in the MW-frequency regime [27,28,67] and these results could position N-V ensembles as a practical platform for high-frequency sensing applications, including microwave-circuitry imaging [23] and near-field antenna characterization [24]. Extensions of Rabi magnetometry, such as spin locking [65] and quantum frequency mixing [66], can be implemented in these devices to further widen the application space by opening up new frequency ranges for high-sensitivity diamond-based magnetometry.

ACKNOWLEDGMENTS

We thank A. Libson, C. Hart, J. T. Oon, and Y. Liu for helpful comments and discussions. We also thank L. Pham for strain-gradient measurements of the diamond. This work was supported in part by the Q-Diamond Grant No. W911NF13D0001. S.A. was supported by the National Science Foundation (NSF) through the NSF Graduate Research Fellowship Program.

Note added.—We recently became aware of similar work reporting MW sensing with 8.9-pT/ $\sqrt{\text{Hz}}$ sensitivity [68].

- [1] C. L. Degen, F. Reinhard, and P. Cappellaro, Quantum sensing, *Rev. Mod. Phys.* **89**, 035002 (2017).
- [2] D. Budker and M. Romalis, Optical magnetometry, *Nat. Phys.* **3**, 227 (2007).
- [3] K.-M. C. Fu, G. Z. Iwata, A. Wickenbrock, and D. Budker, Sensitive magnetometry in challenging environments, *AVS Quantum Sci.* **2**, 044702 (2020).
- [4] M. W. Doherty, N. B. Manson, P. Delaney, F. Jelezko, J. Wrachtrup, and L. C. Hollenberg, The nitrogen-vacancy colour centre in diamond, *Phys. Rep.* **528**, 1 (2013).
- [5] G. Balasubramanian, P. Neumann, D. Twitchen, M. Markham, R. Kolesov, N. Mizuochi, J. Isoya, J. Achard, J. Beck, J. Tissler, V. Jacques, P. R. Hemmer, F. Jelezko, and J. Wrachtrup, Ultralong spin coherence time in isotopically engineered diamond, *Nat. Mater.* **8**, 383 (2009).
- [6] E. V. Levine, M. J. Turner, P. Kehayias, C. A. Hart, N. Langellier, R. Trubko, D. R. Glenn, R. R. Fu, and R. L. Walsworth, Principles and techniques of the quantum diamond microscope, *Nanophotonics* **8**, 1945 (2019).
- [7] J. M. Schloss, J. F. Barry, M. J. Turner, and R. L. Walsworth, Simultaneous Broadband Vector Magnetometry Using Solid-State Spins, *Phys. Rev. Appl.* **10**, 034044 (2018).
- [8] D. M. Toyli, D. J. Christle, A. Alkauskas, B. B. Buckley, C. G. Van de Walle, and D. D. Awschalom, Measurement and Control of Single Nitrogen-Vacancy Center Spins above 600 K, *Phys. Rev. X* **2**, 031001 (2012).
- [9] M. W. Doherty, V. V. Struzhkin, D. A. Simpson, L. P. McGuinness, Y. Meng, A. Stacey, T. J. Karle, R. J. Hemley, N. B. Manson, L. C. L. Hollenberg, and S. Prawer, Electronic Properties and Metrology Applications of the Diamond NV⁻ Center under Pressure, *Phys. Rev. Lett.* **112**, 047601 (2014).
- [10] J. F. Barry, M. J. Turner, J. M. Schloss, D. R. Glenn, Y. Song, M. D. Lukin, H. Park, and R. L. Walsworth, Optical magnetic detection of single-neuron action potentials using quantum defects in diamond, *Proc. Natl. Acad. Sci.* **113**, 14133 (2016).
- [11] D. R. Glenn, D. B. Bucher, J. Lee, M. D. Lukin, H. Park, and R. L. Walsworth, High-resolution magnetic resonance spectroscopy using a solid-state spin sensor, *Nature* **555**, 351 (2018).
- [12] I. Lovchinsky, A. O. Sushkov, E. Urbach, N. P. de Leon, S. Choi, K. De Greve, R. Evans, R. Gertner, E. Bersin, C. Müller, L. McGuinness, F. Jelezko, R. L. Walsworth, H. Park, and M. D. Lukin, Nuclear magnetic resonance detection and spectroscopy of single proteins using quantum logic, *Science* **351**, 836 (2016).
- [13] F. Casola, T. van der Sar, and A. Yacoby, Probing condensed matter physics with magnetometry based on nitrogen-vacancy centres in diamond, *Nat. Rev. Mater.* **3**, 17088 (2018).
- [14] D. R. Glenn, R. R. Fu, P. Kehayias, D. Le Sage, E. A. Lima, B. P. Weiss, and R. L. Walsworth, Micrometer-scale magnetic imaging of geological samples using a quantum diamond microscope, *Geochem. Geophys. Geosyst.* **18**, 3254 (2017).
- [15] T. Fleig and P. Frontera, in *2018 IEEE/ION Position, Location and Navigation Symposium (PLANS)* (IEEE, Monterey, CA, USA, 2018), p. 1107.
- [16] P. Frontera and S. Alessandrini, in *Proceedings of the ION 2019 Pacific PNT Meeting, Honolulu, Hawaii* (Institute of Navigation, 2019), p. 886.
- [17] J. F. Barry, J. M. Schloss, E. Bauch, M. J. Turner, C. A. Hart, L. M. Pham, and R. L. Walsworth, Sensitivity optimization for NV-diamond magnetometry, *Rev. Mod. Phys.* **92**, 015004 (2020).

- [18] I. Fescenko, A. Jarmola, I. Savukov, P. Kehayias, J. Smits, J. Damron, N. Ristoff, N. Mosavian, and V. M. Acosta, Diamond magnetometer enhanced by ferrite flux concentrators, *Phys. Rev. Res.* **2**, 023394 (2020).
- [19] E. R. Eisenach, J. F. Barry, M. F. O'Keeffe, J. M. Schloss, M. H. Steinecker, D. R. Englund, and D. A. Braje, Cavity-enhanced microwave readout of a solid-state spin sensor, *Nat. Commun.* **12**, 094705 (2021).
- [20] J. F. Barry, M. H. Steinecker, S. T. Alsid, J. Majumder, L. M. Pham, M. F. O'Keefe, and D. A. Braje, Sensitive ac and dc magnetometry with nitrogen-vacancy center ensembles in diamond (2023), [arXiv:2305.06269](https://arxiv.org/abs/2305.06269) [quantph].
- [21] D. Le Sage, L. M. Pham, N. Bar-Gill, C. Belthangady, M. D. Lukin, A. Yacoby, and R. L. Walsworth, Efficient photon detection from color centers in a diamond optical waveguide, *Phys. Rev. B* **85**, 121202 (2012).
- [22] T. Wolf, P. Neumann, K. Nakamura, H. Sumiya, T. Ohshima, J. Isoya, and J. Wrachtrup, Subpicotesla Diamond Magnetometry, *Phys. Rev. X* **5**, 041001 (2015).
- [23] D. A. Anderson, E. Paradis, G. Raithel, R. E. Sapiro, and C. L. Holloway, in *2018 11th Global Symposium on Millimeter Waves (GSMM)* (IEEE, Boulder, CO, 2018), p. 1.
- [24] K. Jomaa, F. Ndagijimana, H. Ayad, M. Fadlallah, and J. Jomaah, in *2017 International Symposium on Electromagnetic Compatibility—EMC EUROPE* (IEEE, Angers, France, 2017), p. 4.
- [25] P. M. Holl and F. Reinhard, Holography of Wi-Fi Radiation, *Phys. Rev. Lett.* **118**, 183901 (2017).
- [26] D. H. Meyer, K. C. Cox, F. K. Fatemi, and P. D. Kunz, Digital communication with Rydberg atoms and amplitude-modulated microwave fields, *Appl. Phys. Lett.* **112**, 211108 (2018).
- [27] L. Shao, R. Liu, M. Zhang, A. V. Shneidman, X. Audier, M. Markham, H. Dhillon, D. J. Twitchen, Y.-F. Xiao, and M. Lončar, Wide-field optical microscopy of microwave fields using nitrogen-vacancy centers in diamonds, *Adv. Opt. Mater.* **4**, 1075 (2016).
- [28] A. Horsley, P. Appel, J. Wolters, J. Achard, A. Tallaire, P. Maletinsky, and P. Treutlein, Microwave Device Characterization Using a Widefield Diamond Microscope, *Phys. Rev. Appl.* **10**, 044039 (2018).
- [29] J.-M. Cai, B. Naydenov, R. Pfeiffer, L. P. McGuinness, K. D. Jahnke, F. Jelezko, M. B. Plenio, and A. Retzker, Robust dynamical decoupling with concatenated continuous driving, *New J. Phys.* **14**, 113023 (2012).
- [30] A. Stark, N. Aharon, T. Unden, D. Louzon, A. Huck, A. Retzker, U. L. Andersen, and F. Jelezko, Narrow-bandwidth sensing of high-frequency fields with continuous dynamical decoupling, *Nat. Commun.* **8**, 1 (2017).
- [31] T. Joas, A. M. Waeber, G. Braunbeck, and F. Reinhard, Quantum sensing of weak radio-frequency signals by pulsed mollow absorption spectroscopy, *Nat. Commun.* **8**, 964 (2017).
- [32] G. Wang, Y.-X. Liu, and P. Cappellaro, Coherence protection and decay mechanism in qubit ensembles under concatenated continuous driving, *New J. Phys.* **22**, 123045 (2020).
- [33] J. Meinel, V. Vorobyov, B. Yavkin, D. Desari, H. Sumiya, S. Onoda, J. Isoya, and J. Wrachtrup, Heterodyne sensing of microwaves with a quantum sensor, *Nat. Commun.* **12**, 2737 (2021).
- [34] I. I. Rabi, Space quantization in a gyrating magnetic field, *Phys. Rev.* **51**, 652 (1937).
- [35] F. Jelezko, T. Gaebel, I. Popa, A. Gruber, and J. Wrachtrup, Observation of Coherent Oscillations in a Single Electron Spin, *Phys. Rev. Lett.* **92**, 076401 (2004).
- [36] F. Yan, S. Gustavsson, J. Bylander, X. Jin, F. Yoshihara, D. G. Cory, Y. Nakamura, T. P. Orlando, and W. D. Oliver, Rotating-frame relaxation as a noise spectrum analyser of a superconducting qubit undergoing driven evolution, *Nat. Commun.* **4**, 2337 (2013).
- [37] E. Geva, R. Kosloff, and J. L. Skinner, On the relaxation of a two-level system driven by a strong electromagnetic field, *J. Chem. Phys.* **102**, 8541 (1995).
- [38] See the Supplemental Material at <http://link.aps.org/supplemental/10.1103/PhysRevApplied.19.054095> for more details on simulations and experiments.
- [39] L. Robledo, H. Bernien, T. V. D. Sar, and R. Hanson, Spin dynamics in the optical cycle of single nitrogen-vacancy centres in diamond, *New J. Phys.* **13**, 025013 (2011).
- [40] J.-P. Tetienne, L. Rondin, P. Spinicelli, M. Chipaux, T. Debuisschert, J.-F. Roch, and V. Jacques, Magnetic-field-dependent photodynamics of single NV defects in diamond: An application to qualitative all-optical magnetic imaging, *New J. Phys.* **14**, 103033 (2012).
- [41] G. Davies and M. F. Hamer, Optical studies of the 1.945 eV vibronic band in diamond, *Proc. R. Soc. London, A* **348**, 285 (1976).
- [42] V. M. Acosta, E. Bauch, M. P. Ledbetter, A. Waxman, L.-S. Bouchard, and D. Budker, Temperature Dependence of the Nitrogen-Vacancy Magnetic Resonance in Diamond, *Phys. Rev. Lett.* **104**, 070801 (2010).
- [43] L. J. Rogers, M. W. Doherty, M. S. J. Barson, S. Onoda, T. Ohshima, and N. B. Manson, Singlet levels of the NV-centre in diamond, *New J. Phys.* **17**, 013048 (2015).
- [44] T. Teraji, T. Taniguchi, S. Koizumi, Y. Koide, and J. Isoya, Effective use of source gas for diamond growth with isotopic enrichment, *Appl. Phys. Express* **6**, 055601 (2013).
- [45] T. Teraji, T. Yamamoto, K. Watanabe, Y. Koide, J. Isoya, S. Onoda, T. Ohshima, L. J. Rogers, F. Jelezko, P. Neumann, J. Wrachtrup, and S. Koizumi, Homoepitaxial diamond film growth: High purity, high crystalline quality, isotopic enrichment, and single color center formation, *Phys. Status Solidi (a)* **212**, 2365 (2015).
- [46] P. Kehayias, M. J. Turner, R. Trubko, J. M. Schloss, C. A. Hart, M. Wesson, D. R. Glenn, and R. L. Walsworth, Imaging crystal stress in diamond using ensembles of nitrogen-vacancy centers, *Phys. Rev. B* **100**, 174103 (2019).
- [47] H. Clevenson, M. E. Trusheim, C. Teale, T. Schroder, D. Braje, and D. Englund, Broadband magnetometry and temperature sensing with a light-trapping diamond waveguide, *Nat. Phys.* **11**, 393 (2015).
- [48] R. de Sousa, in *Electron Spin Resonance and Related Phenomena in Low-Dimensional Structures* (Springer-Verlag, Berlin, Heidelberg, 2009), p. 183.
- [49] J. F. Hoburg, Principles of quasistatic magnetic shielding with cylindrical and spherical shields, *IEEE Trans. Electromagn. Compat.* **37**, 574 (1995).

- [50] E. R. Eisenach, J. F. Barry, L. M. Pham, R. G. Rojas, D. R. Englund, and D. A. Braje, Broadband loop gap resonator for nitrogen vacancy centers in diamond, *Rev. Sci. Instrum.* **89**, 094705 (2018).
- [51] F. L. Goerner, T. Duong, R. J. Stafford, and G. D. Clarke, A comparison of five standard methods for evaluating image intensity uniformity in partially parallel imaging MRI, *Med. Phys.* **40**, 082302 (2013).
- [52] N. Bar-Gill, L. M. Pham, A. Jarmola, D. Budker, and R. L. Walsworth, Solid-state electronic spin coherence time approaching one second, *Nat. Commun.* **4**, 1743 (2013).
- [53] H. J. Mamin, M. H. Sherwood, M. Kim, C. T. Rettner, K. Ohno, D. D. Awschalom, and D. Rugar, Multipulse Double-Quantum Magnetometry with Near-Surface Nitrogen-Vacancy Centers, *Phys. Rev. Lett.* **113**, 030803 (2014).
- [54] C. A. Hart, J. M. Schloss, M. J. Turner, P. J. Scheidegger, E. Bauch, and R. L. Walsworth, N-V-Diamond Magnetic Microscopy Using a Double Quantum 4-Ramsey Protocol, *Phys. Rev. Appl.* **15**, 044020 (2021).
- [55] S. Felton, B. L. Cann, A. M. Edmonds, S. Liggins, R. J. Cruddace, M. E. Newton, D. Fisher, and J. M. Baker, Electron paramagnetic resonance studies of nitrogen interstitial defects in diamond, *J. Phys.: Condens. Matter* **eid 21**, 364212 (2009).
- [56] M. W. Doherty, F. Dolde, H. Fedder, F. Jelezko, J. Wrachtrup, N. B. Manson, and L. C. L. Hollenberg, Theory of the ground-state spin of the NV⁻ center in diamond, *Phys. Rev. B* **85**, 205203 (2012).
- [57] S. Felton, A. M. Edmonds, M. E. Newton, P. M. Martineau, D. Fisher, D. J. Twitchen, and J. M. Baker, Hyperfine interaction in the ground state of the negatively charged nitrogen vacancy center in diamond, *Phys. Rev. B* **79**, 075203 (2009).
- [58] J. T. Oon, J. Tang, C. A. Hart, K. S. Olsson, M. J. Turner, J. M. Schloss, and R. L. Walsworth, Ramsey envelope modulation in NV diamond magnetometry, *Phys. Rev. B* **106**, 054110 (2022).
- [59] T. Gaebel, M. Domhan, I. Popa, C. Wittmann, P. Neumann, F. Jelezko, J. R. Rabeau, N. Stavrias, A. D. Greentree, and S. Prawer, *et al.*, Room-temperature coherent coupling of single spins in diamond, *Nat. Phys.* **2**, 408 (2006).
- [60] K. Ohno, F. Joseph Heremans, L. C. Bassett, B. A. Myers, D. M. Toyli, A. C. Bleszynski Jayich, C. J. Palmstrøm, and D. D. Awschalom, Engineering shallow spins in diamond with nitrogen delta-doping, *Appl. Phys. Lett.* **101**, 082413 (2012).
- [61] H.-J. Kim, H. Hirayama, S. Kim, K. J. Han, R. Zhang, and J.-W. Choi, Review of near-field wireless power and communication for biomedical applications, *IEEE Access* **5**, 21264 (2017).
- [62] D. Farfurnik, N. Aharon, I. Cohen, Y. Hovav, A. Retzker, and N. Bar-Gill, Experimental realization of time-dependent phase-modulated continuous dynamical decoupling, *Phys. Rev. A* **96**, 013850 (2017).
- [63] S. T. Alsid, J. F. Barry, L. M. Pham, J. M. Schloss, M. F. O'Keeffe, P. Cappellaro, and D. A. Braje, Photoluminescence Decomposition Analysis: A Technique to Characterize N-V Creation in Diamond, *Phys. Rev. Appl.* **12**, 044003 (2019).
- [64] V. Stepanov, F. H. Cho, C. Abeywardana, and S. Takahashi, High-frequency and high-field optically detected magnetic resonance of nitrogen-vacancy centers in diamond, *Appl. Phys. Lett.* **106**, 063111 (2015).
- [65] M. Loretz, T. Rosskopf, and C. L. Degen, Radio-Frequency Magnetometry Using a Single Electron Spin, *Phys. Rev. Lett.* **110**, 017602 (2013).
- [66] G. Wang, Y.-X. Liu, J. M. Schloss, S. T. Alsid, D. A. Braje, and P. Cappellaro, Sensing of Arbitrary-Frequency Fields Using a Quantum Mixer, *Phys. Rev. X* **12**, 021061 (2022).
- [67] P. Wang, Z. Yuan, P. Huang, X. Rong, M. Wang, X. Xu, C. Duan, C. Ju, F. Shi, and J. Du, High-resolution vector microwave magnetometry based on solid-state spins in diamond, *Nat. Commun.* **6**, 1 (2015).
- [68] Z. Wang, F. Kong, P. Zhao, Z. Huang, P. Yu, Y. Wang, F. Shi, and J. Du, Picotesla magnetometry of microwave fields with diamond sensors, *Sci. Adv.* **8**, eabq8158 (2022).